第 43 卷 第 16 期/2023 年 8 月/光学学报 研究论文

光学学报

基于亚波长尺寸微纳光纤的光热光谱NH_3检测

郑毅，郭安波，曾祥龙*

上海大学特种光纤与光接入网重点实验室，特种光纤与先进通信国际联合研究实验室，上海 200444

摘要 在通信波段研究了基于亚波长尺寸微纳光纤的光热光谱气体传感技术，利用锥腰直径为1 μm的微纳光纤代替传统的自由空间光气室和空芯光纤实现紧凑的全光纤结构，其引导的倏逝场被气体吸收后会激发光热效应。仿真结果表明，约25%的光波以倏逝场的形式沿光纤表面传播，可提供的光热效应强度约为空芯光纤的187倍。通过外差干涉法在微纳光纤提供的4 mm超短有效传感光程上实现了1512.24 nm处10^{-6}级别氨气(NH_3)检测。当使用的泵浦光功率为3.6 mW时，得到1σ噪声等效检测下限为39×10^{-6}，30个泵浦调谐周期内探测信号的不稳定性小于0.5%。

关键词 光谱学；光热光谱；微纳光纤；外差干涉；光纤传感器；NH_3检测

中图分类号 TN25 **文献标志码** A **DOI**：10.3788/AOS230848

1 引 言

光热光谱(PTS)技术具有低检测限、高选择性和强鲁棒性等特点[1-3]，是一种新颖且高效灵活的二阶传感技术[4-7]。PTS系统通常采用“泵浦-探测”双光源结构，通过光热效应将由气体非线性吸收泵浦光导致的功率变化编码到探测光相位上[8-9]，随后使用一个外差[10]或零差[11]干涉仪来获取相位的波动，并使用一个锁相放大器(LIA)解调出谐波信号[12]。与传统的可调谐半导体激光吸收光谱(TDLAS)技术[13]相比，PTS技术在近红外波段对弱吸收气体(如氨气)进行检测时，干涉结构的使用以及对相位的精确解调使其能够在更短的有效传感光程上得到更高的灵敏度。得益于此，PTS系统可以被灵活地部署在各种复杂环境中，在变压器油气检测[14]、呼吸气体分析[3]等场景具有较高的应用价值。

近年来，空芯光纤(HCF)被证明能有效替代传统的自由空间光气室[15-17]，在保证低检测限的同时能够实现全光纤结构[18]，其已被广泛地应用于PTS系统中。然而，由于狭长的空气芯需要被待测气体均匀填充，气体缓慢的自由扩散势必导致难以实现实时监测[14]。Jin等[19]通过在HCF表面进行局部钻孔有效地缩短了气体填充空气芯的时间，利用高压气泵辅助可以得到秒级别的响应。然而，微纳尺度的精密操作不仅富有挑战性，还使得传感元件的成本急剧攀升，能够引导高能量密度倏逝场的亚波长尺寸微纳光纤很适合被用作高灵敏、低成本的紧凑型PTS气体检测系统的核心传感元件[20]。

本文搭建了基于微纳光纤的外差干涉式PTS系统，将通过熔融拉锥法制成的直径为1 μm的微纳光纤作为核心传感元件。通过波长为1550 nm的探测光来感知中心波长为1512 nm、平均功率为3.6 mW的泵浦光激发的光热效应。通过对干涉仪输出的拍频信号进行解调，在4 mm的超短有效传感光程上得到氨气(NH_3)的1σ检测下限为39×10^{-6}，30个泵浦光调谐周期内的探测信号波动小于0.5%。实验结果表明，所搭建系统能够对10^{-6}级别的NH_3进行有效响应，且具备一定的抗振动干扰能力，可为未来复杂环境中的气体检测提供高灵敏、高集成且经济实惠的解决方案。

2 实验设计

2.1 原理分析与仿真

在PTS系统中，气体分子吸收泵浦光时会周期性地加热局部传感介质，此时介质折射率会呈现周期性调制。这将导致与泵浦光共线传播的探测光的相位也被相应地调制，调制强度与体热源大小呈正相关。由气体分子热弛豫过程产生的体热源[21]可以表示为

$$Q(r,t)=\alpha\cdot P_{\mathrm{pump}}\cdot D_{\mathrm{pump}}(r)\cdot M(t), \tag{1}$$

式中：α、P_{pump}和$M(t)$分别为气体分子峰值吸收系数、泵浦光平均功率和波长调制波形；$D_{\mathrm{pump}}(r)$为泵浦光归一化强度分布。当泵浦光为基模时，其归一化强度分布[21]可以被进一步描述为

收稿日期：2023-04-19；**修回日期**：2023-06-04；**录用日期**：2023-06-16；**网络首发日期**：2023-07-12

基金项目：上海市科学技术委员会资助项目(20JC1415700)、国家自然科学基金(12274281)、高等学校学科创新引智项目(111计划)(D20031)

通信作者：*zenglong@shu.edu.cn

$$D_{\mathrm{pump}}(r)=\frac{2}{\pi R_{\mathrm{pump}}^2}\exp\left(-2r^2/R_{\mathrm{pump}}^2\right)\propto\frac{1}{R_{\mathrm{pump}}^2},\quad(2)$$

式中：R_{pump}为泵浦光模场的有效半径（功率下降到峰值的$1/e^2$时的半径）。由式（1）、（2）可知，气体分子热弛豫产生的体热源大小与泵浦光能量密度高度相关，其与有效模场半径呈平方反比的关系[22]。对于自由空间或HCF中的光束来说，有效模场直径约为100 μm和10 μm量级，而亚波长尺寸微纳光纤对应的有效模场直径约为1 μm量级甚至更小，因此相较于自由空间和HCF中的光热效应，微纳光纤可以提供2～4个数量级的光热效应提升。与此同时，由于二氧化硅与空气的热光系数（TOC）的绝对值相差约10倍，相同大小的体热源可以使得微纳光纤引导更大的探测光相位调制[20]。这些因素皆说明亚波长尺寸微纳光纤非常适合制成具有高灵敏度的超紧凑PTS气体检测系统。

自2003年Tong等[23]首次制成亚波长尺寸硅基纳米线以来，微纳结构波导逐渐成为小型集成化传感元件的前沿应用平台[24-27]。均匀的锥腰直径、缓变的锥形过渡区与平滑的锥区表面，使得部分光能够以倏逝场的形式沿着光纤表面稳定传输[28]。通过COMSOL软件仿真了不同直径微纳光纤所对应的倏逝场比例以及此时支持的光热效应强度相对于HCF的倍数。

如图1（a）所示，光纤直径被设置成以100 nm为步长，从500 nm增加至3000 nm。通过对时均功率流求表面积分，可以得到倏逝场能量比例随微纳光纤直径减小而呈指数上升的趋势。通过计算微纳光纤和HCF的有效模场区域（此处微纳光纤的模场分为光纤内场与表面倏逝场，HCF的模场直径取10 μm）内的平均功率密度，可以得到二者在相同大小体热源下等效光热效应强度的关系。由于二氧化硅与空气的TOC符号相反（$\varepsilon_{\mathrm{silica}}=9.7\times10^{-6}\sim8.1\times10^{-6}\,\mathrm{K}^{-1}$，$\varepsilon_{\mathrm{air}}=-0.91\times10^{-6}\,\mathrm{K}^{-1}$），因此微纳光纤引导的总折射率调制实际上是光纤内场与倏逝场分别对折射率的影响的差值。当微纳光纤的直径过小时，倏逝场造成的负影响会迅速抵消光纤内场造成的正影响，这会造成总折射率调制量迅速减小；当微纳光纤直径在700 nm左右时[20]，可以获得相对较大的光热效应强度。通过熔融拉锥法制备了绝热型锥形微纳光纤，锥腰直径约为1 μm，均匀锥区长度约为4 mm，锥形过渡区长度约为35 mm。该尺寸下的微纳光纤能够引导约25%的光波以倏逝场的形式在光纤表面传播，其引导的光热效应强度187倍于HCF。在微纳光纤两端接上超连续光源和光谱仪，得到的传输谱如图1（b）所示，其在通信波段处的损耗约为0.75 dB/mm。具有较低损耗并能够支持稳定倏逝场传输的亚波长尺寸微纳光纤为后续实验打下了坚实的基础。

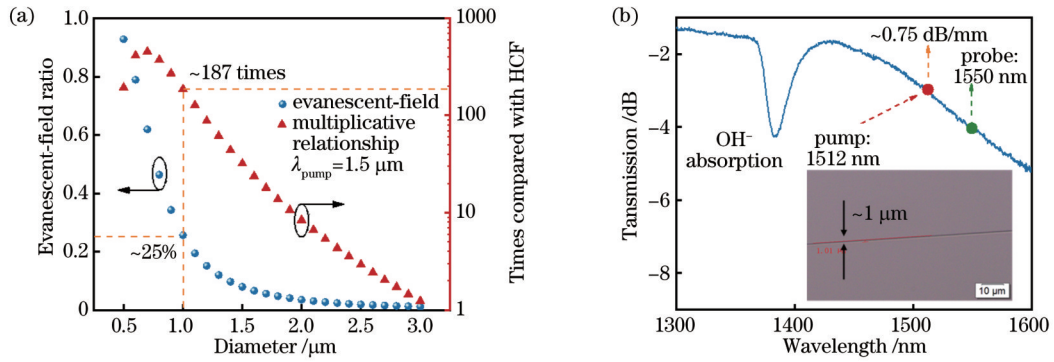

图1　微纳光纤仿真与表征。（a）倏逝场及光热效应仿真；（b）微纳光纤透射谱

Fig. 1　Simulation and characterization of micro-nano fiber. (a) Simulation of evanescent field and photothermal effect; (b) transmission spectrum of fabricated microfiber

2.2　实验系统搭建

基于微纳光纤的PTS检测NH_3的实验装置如图2所示。如图2（a）所示，利用分布式反馈（DFB）激光器（LD-PD INC PL-DFB@1512 nm）和窄线宽激光器（NLL；NKT Photonics E15@1550 nm）分别产生泵浦光和探测光。锁相放大器（LIA；Zurich Instruments UHFLI）产生的三角信号（400 mV，200 mHz）和正弦信号（200 mV，1 kHz）被输入激光控制器并驱动DFB激光器在NH_3吸收线（1512.24 nm，6612.7 cm^{-1}）附近调谐，同时携带频率为1 kHz的高频波长调制。调谐调制的泵浦光经过可调衰减器和环形器的一、二端口后，被引入微纳光纤气室用以激发光热效应。NLL产生的窄线宽探测光被耦合器（OC-1）分成上下两路，上面一路穿过声光调制器（AOM；G&H）并获得80 MHz的光学频移，下面一路被引入微纳光纤气室。此时，附加给探测光的光热相位调制[29-30]在弱吸收条件下可以表示为

$$\Delta\varphi(t)=k\cdot\alpha(\lambda_{\mathrm{pump}})\cdot C\cdot L\cdot P_{\mathrm{pump}}\cdot M(t),\quad(3)$$

式中：k为光热相位调制的转换系数；$\alpha(\lambda_{\mathrm{pump}})$为$NH_3$随泵浦波长变化的吸收系数；$L$表示有效传感长度；$P_{\mathrm{pump}}$和$M(t)$分别表示泵浦光的平均功率和波长调制函数；$C$为气体体积分数。下面一路探测光随后经过环形器的二、三端口，并与携带光学频移的另一路探测光在OC-2中进行混频，再通过一个光电探测器（PD）得到

拍频电信号，此时光热相位调制即被转移到外差频率（80 MHz）处。最终通过LIA对拍频电信号的相位和频率进行连续解调得到二次谐波信号。在该装置中，带通滤波器（BPF-1）被用来防止泵浦光对混频光信号造成干扰，而BPF-2和隔离器（isolator）被用来防止泵浦光和可能的端面反射的探测光损坏NLL。在环形器二端口处测得泵浦光和探测光的平均功率分别为3.6 mW和1.4 mW。

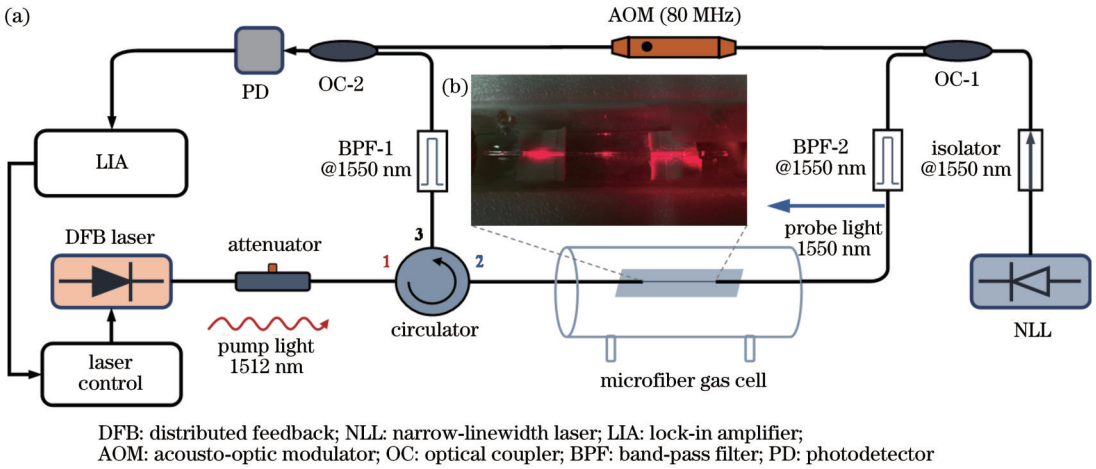

图2　基于亚波长尺寸微纳光纤的PTS气体检测系统。(a)实验框图；(b)微纳光纤引导660 nm可见光

Fig. 2　PTS gas detection system based on microfiber with sub-wavelength dimension. (a) Experimental setup; (b) microfiber guiding 660 nm visible laser

3　结果与分析

3.1　相位调制信号的解调

在图2(a)中，分别携带光学频移和光热相位调制的两路探测光在OC-2中进行混频，拍频信号中心频率为80 MHz，相位调制频率为1 kHz。图3所示为对拍频信号的相位进行解调得到的光热相位调制的时域波形及频谱。

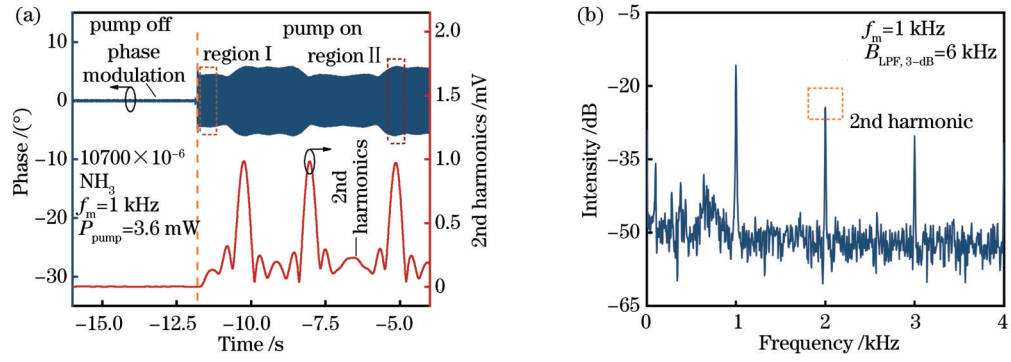

图3　光热相位调制和二次谐波。(a) 泵浦光off/on时的动态过程；(b) 相位调制频谱

Fig. 3　Photothermal phase modulation and second harmonics. (a) Dynamic process when the pump light is off and on; (b) spectrum of phase modulation

当微纳光纤气室中充满体积分数为10700×10^{-6}的NH_3时，研究了由光热效应诱导的探测光相位调制和以此解调出的二次谐波的动态变化过程。当泵浦光关闭时，此时的微纳光纤并没有被加热，因此探测光的相位保持稳定且无法被解调出二次谐波。泵浦光在约−12 s时被打开，其自身的热效应使得微纳光纤被周期性地加热冷却，此时探测光的相位也被相应地调制了，如图3(a)中的region Ⅰ。当泵浦光波长调谐至NH_3的吸收谱线处时，气体分子吸收泵浦光倏逝场所产生的热弛豫后，进一步向微纳光纤传导热量，此时探测光的光热相位调制会被相应地增强，如图3(a)中的region Ⅱ所示。相位调制信号对应的频谱如图3(b)所示，可见其中心频率为1 kHz，而在2 kHz、3 kHz等处的信号皆为region Ⅱ中因气体非线性吸收而激发的谐波信号[30]。

3.2　系统检测性能评估

由于偶次谐波具有轴对称特性，因此选用二次谐波对该系统的性能进行评估。图4所示为在泵浦光调制频率为1 kHz、平均输出功率为3.6 mW时测得的二次谐波。在LIA中，相位解调的参数如下：解调中心频

率为 80 MHz，滤波器截止带宽为 6 kHz；频率解调的参数如下：本振信号频率为 2 kHz，滤波器截止带宽为 2 Hz。

首先，评估当气室中没有 NH_3 时该系统的噪声水平。如图 4(a)中零值附近的黑色曲线所示，对两个泵浦光调谐周期内的噪声值运用 STDEV 函数求得其 1σ 标准差约为 3.4 μV。当微纳光纤气室内充满体积分数为 4280×10^{-6} 到 10700×10^{-6} 的 NH_3 时，对应的解调二次谐波如图 4(a)所示。其中，10700×10^{-6} 时得到的二次谐波峰峰值(V_{pp})为 933.2 μV，与 1σ 噪声的比值为 274.5，被视为该系统的 1σ 噪声等效检测信噪比(SNR)。由此可以估算出该系统的 1σ 噪声等效检测下限约为 39×10^{-6}。对这 4 个二次谐波的幅值进行线性拟合，如图 4(b)所示，其拟合系数 R^2 约为 0.999，可见当 NH_3 的体积分数为 0.4%～1% 时，探测信号幅值与气体体积分数之间具有较好的线性关系。

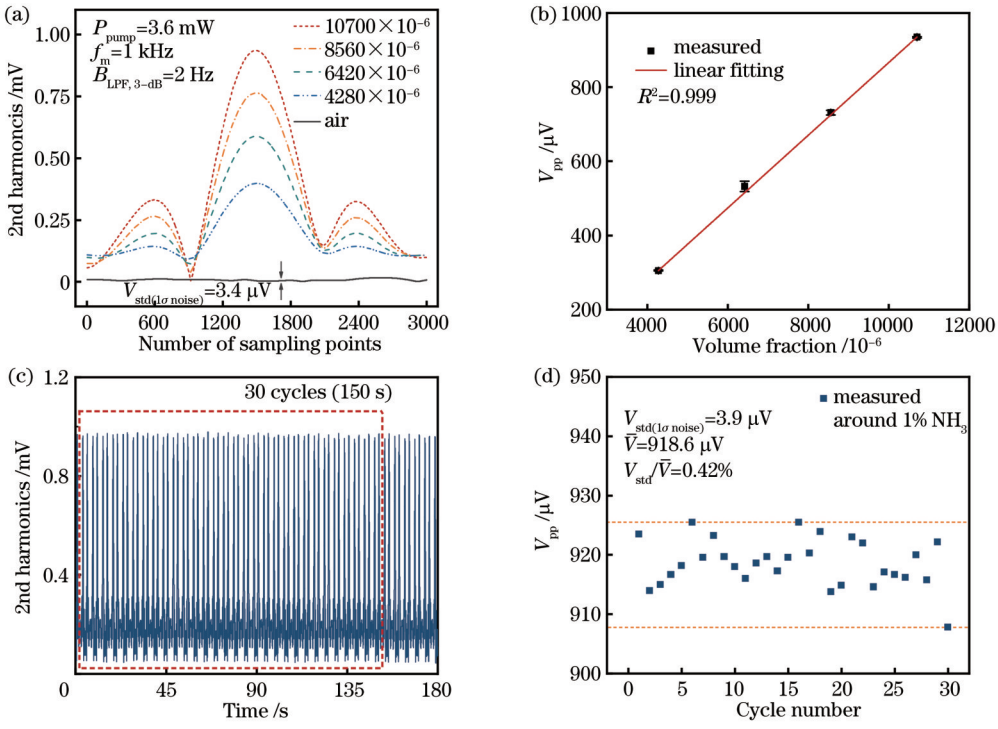

图 4　由二次谐波信号评估系统性能。(a)不同 NH_3 体积分数对应的二次谐波；(b)对峰峰值的线性拟合；(c) 180 s(36 个周期)内的二次谐波波形；(d) 30 个周期内的峰峰值

Fig. 4　Evaluation of system performance by second harmonic signal. (a) Second harmonics corresponding to different NH_3 volume fractions; (b) linear fitting of V_{pp}; (c) second harmonic waveform within 180 s (36 cycles); (d) V_{pp} within 30 cycles

然后，在 NH_3 体积分数为 10700×10^{-6} 时测试了该系统的探测信号稳定性。图 4(c)所示为 180 s(36 个泵浦调谐周期)内的二次谐波波形，前 30 个周期的二次谐波的 V_{pp} 如图 4(d)所示。可以求得该 30 个 V_{pp} 的平均值为 918.6 μV，1σ 标准差为 3.9 μV，二者的比值约为 0.42%。由此求得的较小的标准差系数表明检测信号的幅值较为集中，证明了该系统具有较好的时间稳定性。

3.3　系统其他特性研究

在基于泵浦-探测双光源结构的 PTS 气体传感系统中，系统噪声水平几乎完全取决于探测光和干涉仪本身，而泵浦光功率对其影响甚小。由于解调出的二次谐波与泵浦光之间呈线性响应，因此 PTS 技术允许在一定范围内通过增大泵浦功率来提高检测灵敏度。

此处的泵浦光功率是在 DFB 激光器仅由 200 mV、1 kHz 的正弦信号驱动时在图 2 所示的环形器二端口测得的，其基本代表了入射到微纳光纤锥腰处的功率。通过调节图 2 中的衰减器控制泵浦功率在 1.2～3.6 mW 范围内呈线性梯度分布。在 NH_3 体积分数为 10700×10^{-6} 的条件下，分别记录 5 个不同功率时的二次谐波曲线，如图 5(a)所示，其中 1.2 mW 和 3.6 mW 对应的二次谐波幅值分别约为 316.4 μV 和 933.2 μV，二者相差约 2 倍。当微纳光纤气室中没有 NH_3 时，记录 5 个不同功率下的系统噪声在 10 s(2 个泵浦调谐周期)内的情况，同样分别求得其标准差，并将其与二次谐波的变化绘制在图 5(b)中。可见，随着泵浦功率的线性增大，1σ 噪声值几乎保持不变，而二次谐波幅值呈线性增加，其线性拟合的 R^2 值约为 0.998。1σ 噪声值和二次谐波幅值随泵浦功率的变化以及估算的 1σ 噪声等效检测信噪比如表 1 所示。

最后，研究了基于微纳光纤的 PTS 气体检测系统的抗环境振动干扰的能力。将实验系统固定在光学面包板上，对实验平台施加不同强度的随机敲击，记录此时探测信号的稳定性情况，如图 6 所示。当实验平台

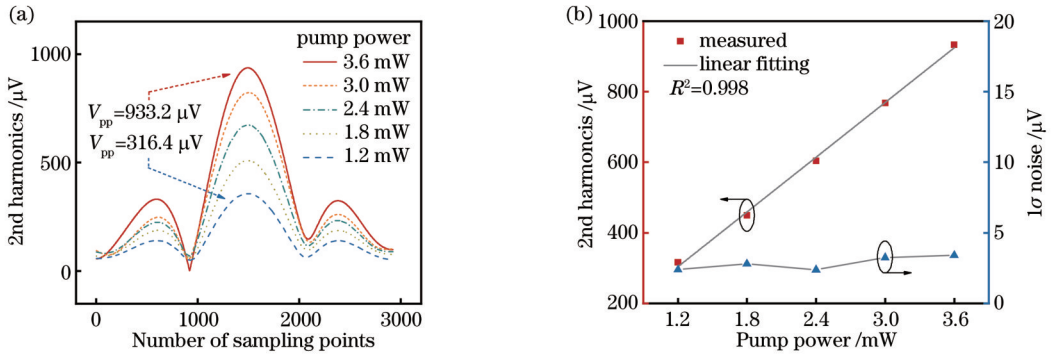

图 5　泵浦功率对检测信噪比的影响。(a)不同泵浦功率对应的二次谐波;(b)不同泵浦功率时信号与 1σ 噪声的比较

Fig. 5　Influence of pump power on SNR. (a) Second harmonics corresponding to different pump power; (b) comparison between signals and 1σ noises at different pump power

表 1　泵浦光功率对检测信噪比的影响

Table 1　Influence of pump power on SNR

Pump power /mW	2nd harmonic / μV	1σ noise /μV	1σ noise equivalent SNR
1.2	316.4	2.39	132.4
1.8	449.5	2.80	160.5
2.4	604.4	2.38	253.9
3.0	768.3	3.25	236.4
3.6	933.2	3.40	274.5

保持稳定时,相位调制的峰峰值约为 8.1°。在 −7.5~−5 s 内对实验平台进行敲击,振动会被传导至微纳光纤上并瞬间改变其微观形貌,因此相位调制信号会在短时间内出现大幅波动,其在 −6.5 s 处的峰峰值约为 131.6°。类比于电路中的非线性负载,由于谐波的激发需要气体分子的非线性吸收,因此图 6 中的二次谐波可以在一定程度的振动干扰下保持稳定,该结果表明 PTS 系统可以满足长期稳定的 10^{-6} 级别 NH_3 检测需求。

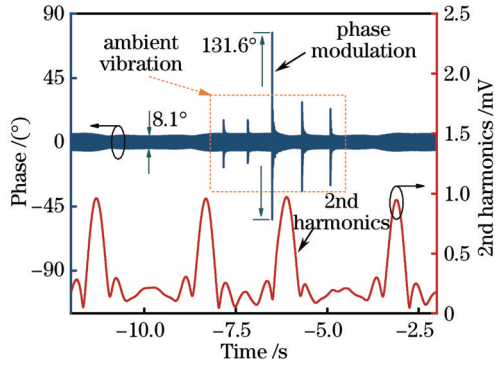

图 6　抗环境振动噪声干扰的能力

Fig. 6　Ability to resist ambient vibration noise

4　结　　论

基于亚波长尺寸微纳光纤实现了 PTS NH_3 传感。首先,制备出直径约为 1 μm 的锥形微纳光纤,仿真结果表明倏逝场约占传输泵浦光能量的 25%,所提供的光热效应强度 187 倍于 HCF。然后,基于此搭建了外差干涉式 PTS 检测系统,通过 4 mm 的超短有效传感光程成功进行了 1512.24 nm 处 10^{-6} 级别的 NH_3 检测。当泵浦光功率为 3.6 mW 时,1σ 噪声等效检测下限为 39×10^{-6},30 个泵浦光调谐周期内探测信号的波动小于 0.5%。研究表明,该 PTS 系统的传感灵敏度可以通过增大泵浦光功率的方法得到提升,并且具备一定程度的对环境振动噪声免疫的能力。该系统具有全光纤超紧凑结构、高灵敏度和低成本等特性,可为复杂环境下的工业过程气体检测提供经济实惠的解决方案。

参　考　文　献

[1] Zhao P C, Zhao Y, Bao H H, et al. Mode-phase-difference photothermal spectroscopy for gas detection with an anti-resonant hollow-core optical fiber[J]. Nature Communications, 2020, 11: 847.

[2] Wang Q, Wang Z, Zhang H, et al. Dual-comb photothermal spectroscopy[J]. Nature Communications, 2022, 13: 2181.

[3] Liu S, Dong X L, Cao H, et al. Mid-infrared photothermal spectroscopy for breath nitric oxide testing with an anti-resonant fiber[J]. Optics & Laser Technology, 2022, 152: 108158.

[4] Bialkowski S E, Astrath N G C, Proskurnin M A. Photothermal spectroscopy methods[M]. Hoboken: Wiley, 2019.

[5] Wei T T, Zifarelli A, Dello Russo S, et al. High and flat spectral responsivity of quartz tuning fork used as infrared photodetector in tunable diode laser spectroscopy[J]. Applied Physics Reviews, 2021, 8(4): 041409.

[6] Pan Y F, Zhao J B, Lu P, et al. All-optical light-induced thermoacoustic spectroscopy for remote and non-contact gas sensing[J]. Photoacoustics, 2022, 27: 100389.

[7] Wu H P, Dong L, Zheng H D, et al. Beat frequency quartz-enhanced photoacoustic spectroscopy for fast and calibration-free continuous trace-gas monitoring[J]. Nature Communications, 2017, 8: 15331.

[8] Zheng K Y, Jiang S L, Chen F F, et al. Mid-infrared all-optical modulators based on an acetylene-filled hollow-core fiber[J]. Light: Advanced Manufacturing, 2022, 3(4): 1-8.

[9] Wang Z, Ren W. Mid-infrared optical modulator enabled by photothermal effect[J]. Light: Science & Applications, 2023, 12: 7.

[10] Krzempek K, Dudzik G, Abramski K, et al. Heterodyne

interferometric signal retrieval in photoacoustic spectroscopy[J]. Optics Express, 2018, 26(2): 1125-1132.
[11] 姜寿林, 靳伟, 陈非凡, 等. 基于空芯光纤光热光谱技术的高灵敏度CO_2检测[J]. 光学学报, 2021, 41(13): 1306004.
Jiang S L, Jin W, Chen F F, et al. Carbon dioxide detection with high sensitivity based on photo-thermal spectroscopy in hollow-core optical fiber[J]. Acta Optica Sinica, 2021, 41(13): 1306004.
[12] Yao C Y, Gao S F, Wang Y Y, et al. Heterodyne interferometric photothermal spectroscopy for gas detection in a hollow-core fiber[J]. Sensors and Actuators B, 2021, 346: 130528.
[13] Viveiros D, Ferreira J, Silva S O, et al. Ammonia sensing system based on wavelength modulation spectroscopy[J]. Photonic Sensors, 2015, 5(2): 109-115.
[14] Ma G M, Wang Y, Chen Z L, et al. Dissolved gas monitoring probe without liquid-gas separation under strong electromagnetic interference[EB/OL]. (2022-03-28) [2023-03-03]. https://arxiv.org/abs/2203.14758.
[15] Krzempek K, Hudzikowski A, Głuszek A, et al. Multi-pass cell-assisted photoacoustic/photothermal spectroscopy of gases using quantum cascade laser excitation and heterodyne interferometric signal detection[J]. Applied Physics B, 2018, 124(5): 74.
[16] Lin Y C, Liu F, He X G, et al. Distributed gas sensing with optical fibre photothermal interferometry[J]. Optics Express, 2017, 25(25): 31568-31585.
[17] 孙亚丽, 朱昕玥, 吴达坤, 等. 基于反谐振空芯光纤的中红外TDLAS系统设计及应用实验研究[J]. 光学学报, 2023, 43(13): 1306005.
Sun Y L, Zhu X Y, Wu D K, et al. Design and experimental study of mid-infrared TDLAS system based on anti-resonant hollow core fiber[J]. Acta Optica Sinia, 2023, 43(13): 1306005.
[18] 斯贝贝, 刘家祥, 司赶上, 等. 基于反谐振空芯光纤的甲烷气体检测[J]. 光学学报, 2022, 42(19): 1906003.
Si B B, Liu J X, Si G S, et al. Methane gas detection based on anti-resonant hollow-core fiber[J]. Acta Optica Sinica, 2022, 42(19): 1906003.
[19] Jin W, Cao Y C, Yang F, et al. Ultra-sensitive all-fibre photothermal spectroscopy with large dynamic range[J]. Nature Communications, 2015, 6: 6767.
[20] Qi Y, Yang F, Lin Y C, et al. Nanowaveguide enhanced photothermal interferometry spectroscopy[J]. Journal of Lightwave Technology, 2017, 35(24): 5267-5275.
[21] Lin Y C, Jin W, Yang F, et al. Pulsed photothermal interferometry for spectroscopic gas detection with hollow-core optical fibre[J]. Scientific Reports, 2016, 6(1): 1-12.
[22] Bao H H, Hong Y Z, Jin W, et al. Modeling and performance evaluation of in-line Fabry-Perot photothermal gas sensors with hollow-core optical fibers[J]. Optics Express, 2020, 28(4): 5423-5435.
[23] Tong L M, Gattass R R, Ashcom J B, et al. Subwavelength-diameter silica wires for low-loss optical wave guiding[J]. Nature, 2003, 426(6968): 816-819.
[24] Hu M P, Zhang H, Wang W B, et al. Micro-nano fiber-assisted active photoacoustic spectroscopy for gas sensing[J]. Optics Express, 2023, 31(2): 3278-3290.
[25] 张伟建, 曾祥龙, 杨傲, 等. 纳米金涂覆微纳光纤的倏逝场氨气检测研究[J]. 光电工程, 2021, 48(9): 200451.
Zhang W J, Zeng X L, Yang A, et al. Research on evanescent field ammonia detection with gold-nanosphere coated microfibers [J]. Opto-Electronic Engineering, 2021, 48(9): 200451.
[26] 王硕, 蒋源, 崔帅威, 等. 基于TDLAS的纳米光纤甲烷传感器[J]. 激光与光电子学进展, 2023, 60(6): 0628011.
Wang S, Jiang Y, Cui S W, et al. Nanofiber methane sensor based on TDLAS technology[J]. Laser & Optoelectronics Progress, 2023, 60(6): 0628011.
[27] He Y, Ma Y F, Tong Y, et al. Long distance, distributed gas sensing based on micro-nano fiber evanescent wave quartz-enhanced photoacoustic spectroscopy[J]. Applied Physics Letters, 2017, 111(24): 241102.
[28] Harrington K, Yerolatsitis S, van Ras D, et al. Endlessly adiabatic fiber with a logarithmic refractive index distribution[J]. Optica, 2017, 4(12): 1526-1533.
[29] Chen F F, Jiang S L, Jin W, et al. Ethane detection with mid-infrared hollow-core fiber photothermal spectroscopy[J]. Optics Express, 2020, 28(25): 38115-38126.
[30] Krzempek K. Part-per-billion level photothermal nitric oxide detection at 5.26 μm using antiresonant hollow-core fiber-based heterodyne interferometry[J]. Optics Express, 2021, 29(20): 32568-32579.

Photothermal Spectroscopy NH_3 Detection Based on a Microfiber with Sub-Wavelength Dimension

Zhu Yi, Guo Anbo, Zeng Xianglong*

Key Lab of Specialty Fiber Optics and Optical Access Network, Joint International Research Laboratory of Specialty Fiber Optics and Advanced Communication, Shanghai University, Shanghai 200444, *China*

Abstract

Objective Gas sensing technology based on spectral absorption has been widely employed in various domains, such as industrial manufacturing and biomedical applications. Nevertheless, due to the constraints imposed by the Lambert-Beer law, the detection of weakly absorbing gases (such as ammonia) in the near-infrared (NIR) bands often necessitates the auxiliary utilization of multi-pass cells with ultra-long optical paths. This inevitably brings about a significant increase in equipment size and substantial manufacturing and operational costs. In recent years, it has been discovered that the photothermal spectroscopy (PTS) technique can compensate for the limitations of conventional spectral absorption-based gas sensing technologies, leading to extensive studies in this field. PTS adopts a pump-probe dual-light configuration, and

the photothermal effect (PTE) induced by the non-radiative relaxation of gas molecules encodes the pump-light power variation onto the phase of the probe light. Subsequently, the phase fluctuation is extracted through a heterodyne or homodyne interferometer, and harmonic signals are demodulated through a lock-in amplifier. The PTE intensity (probe-light phase modulation) in the PTS system is directly related to the pump power density. As a result, the PTS system can achieve higher sensitivity on a much shorter sensing path, thus significantly reducing the equipment volume and costs. Hollow-core fiber (HCF), has been widely applied in PTS systems to realize ultra-sensitive sensing, benefiting from its capability to guide high power density. However, the sensing chamber formed by the elongated air core within the HCF needs to be uniformly filled with the target gas which hinders the real-time detection. The solution of drilling micro holes on the HCF surface using a femtosecond laser has emerged. With the assistance of a miniaturized high-pressure gas pump, this approach reduces the time required for filling the gas into the HCF and achieves a response time in dozens of seconds. Performing micron-level local drilling on the HCF places high demands on the fabrication process and leads to a sharp increase in costs undeniably. Therefore, the solution to high sensitivity, high integration, and low fabrication costs in sensing elements is crucial for the commercial application of PTS technology. Microfiber featuring high-power density, compact size, and cost-effective fabrication, can serve as an effective alternative.

Methods We employ a tapered microfiber as the sensing element in the PTS system. Firstly, by building a cross-sectional model of microfiber-air in COMSOL and calculating the surface integration of the time-averaged power flux in different areas, the relationship between the evanescent field proportion and the microfiber diameter could be obtained. Based on the evanescent field proportion, the average power density of the in-fiber field and the evanescent field could be estimated. By utilizing the thermal-optic coefficients of air and SiO_2, the equivalent PTE intensity with varying diameters could be calculated and compared with the PTE intensity in the HCF. Subsequently, a tapered microfiber is fabricated through the fusion tapering approach and then encapsulated in a glass jar to form a gas chamber. Finally, the chamber is incorporated into the PTS system. The pump is tuned around 1512.24 nm (the NH_3 absorption line), while the center wavelength of the probe is 1550 nm. The average powers for the pump and probe are 3.6 mW and 1.4 mW respectively.

Results and Discussions The tapered microfiber, with a waist diameter of 1 μm and a waist length of about 4 mm, exhibits an insertion loss of 0.75 dB/mm at the communication band (Fig. 1). The simulation results show that the evanescent field accounts for about 25% of the propagating pump light, providing a PTE intensity approximately 187 times higher than that of the HCF (Fig. 1). A heterodyne PTS gas sensing system is constructed by employing a microfiber as the key component (Fig. 2). A detailed analysis in both the frequency and time domains is conducted to examine the dynamic variations of the photothermal phase modulation during gas absorption (Fig. 3). The phase modulation intensities are found to be 8.1° and 11.6° when the pump scans away and is at the NH_3 absorption line respectively. Based on the demodulated second harmonics under the 10700×10^{-6} NH_3 volume fraction and the noise, the 1σ equivalent detection limit of 39×10^{-6} is obtained (Fig. 4). By calculating the 1σ standard deviation of the second harmonics over 30 pump scanning cycles, the system instability is 0.42% (Fig. 4). Additionally, by increasing the pump power from 1.2 mW to 3.6 mW and considering the corresponding noise and second harmonics, it is validated that the SNR can be enhanced by increasing the pump power (Fig. 5). Finally, through applying random vibration excitation to the system, the phase modulation amplitude increases by approximately 16 times during the occurrence of vibration, while the second harmonics remains stable. This demonstrates the system′s ability to withstand ambient vibration noise.

Conclusions Our study investigates PTS gas detection based on microfiber at the communication band with NH_3 as the target gas. Firstly, a tapered microfiber with a diameter of 1 μm is fabricated. The simulation indicates that the evanescent field accounts for about 25% of the pump power, bringing about a PTE intensity 187 times higher than that of HCF. Subsequently, a heterodyne PTS detection system is constructed. NH_3 detection under the 10^{-6} level at 1512.24 nm is achieved with an ultra-short sensing length of 4 mm. With a pump power of 3.6 mW, the 1σ noise equivalent detection limit of 39×10^{-6} is realized, and the instability of the detection signal within 30 pump tuning cycles is less than 0.5%. This system has a certain degree of immunity to ambient vibration, and the sensing sensitivity could be increased by boosting the pump power. The all-fiber, ultra-compact structure, high sensitivity, and low-cost characteristics make this system an affordable solution for gas detection in complex industrial processes.

Key words spectroscopy; photothermal spectroscopy; microfiber; heterodyne interference; fiber optics sensors; NH_3 detection